GMR
The Original

EFFECT OF ACR LOADING ON CUO/ZNO PHOTOCATALYSTS FOR SIMULTANEOUS SOLAR HYDROGEN PRODUCTION AND ORGANIC DYE DEGRADATION

Himanshu Yadav[1], Shashank Dubey[2*], Sandip Kumar Singh[3]

[1]Department of Mechanical Engineering, UNSIET, V. B. S. Purvanchal University, Jaunpur, 222003 Uttar Pradesh, India; Email: hy125418@gmail.com
[2*]Department of Mechanical Engineering, UNSIET, V. B. S. Purvanchal University, Jaunpur, 222003 Uttar Pradesh, India. Email: shashank.dubey001@gmail.com; ORCID : 0009-0006-0729-4760
[3]Department of Mechanical Engineering, UNSIET, V. B. S. Purvanchal University, Jaunpur, 222003 Uttar Pradesh, India. Email: singhsandipkumar25@gmail.com
*Corresponding Author: Email: shashank.dubey001@gmail.com

ABSTRACT
The design of multifunctional photocatalysts capable of simultaneously facilitating solar driven hydrogen production and organic pollutant degradation is pivotal for addressing global energy and environmental challenges. In this study, CuO/ZnO nanocomposites modified with 1% by weight activated carbon rings (ACR) were synthesized via a hydrothermal route and systematically characterized using XRD, SEM, FT-IR, UV-Vis, and photoluminescence spectroscopy. Among the prepared nanocomposites, the sample containing 1 wt% ACR demonstrated superior photocatalytic activity, achieving a hydrogen evolution rate of 29,500 ± 1215.4 μmol g-1h-1 using a 1:1 sacrificial agent mixture, and attaining 95% degradation of methylene blue within 60 minutes under simulated solar light. Enhanced performance is attributed to improved charge carrier separation, increased visible-light absorption, and the formation of efficient hetero junctions. These results underscore the critical importance of ACR loading to maximize the dual functionality of CuO/ZnO based photocatalysts for sustainable solar hydrogen generation and wastewater remediation.

KEYWORDS: Hydrogen production, water electrolysis, clean energy, environmental remediation, Activated Carbon Rings.

INTRODUCTION

The growing global demand for clean energy and the increasing concern over environmental pollution have driven intensive research into multifunctional photocatalysts capable of addressing both challenges simultaneously. Solar-driven hydrogen production via photocatalytic water splitting is considered a promising pathway for sustainable energy generation, offering a carbon-free, abundant, and renewable energy source [1]. Concurrently, the photocatalytic degradation of organic dyes and pollutants is vital for wastewater treatment, particularly in textile, pharmaceutical, and chemical industries [2]. Zinc oxide (ZnO), a wide band gap semiconductor (3.2 eV), has been extensively explored for photocatalysis due to its stability, abundance, and non-toxicity [3]. However, its photocatalytic efficiency is limited by rapid electron-hole recombination and poor visible-light absorption. To overcome these drawbacks, coupling ZnO with copper oxide (CuO), a narrow-band-gap semiconductor (~1.4 eV), has proven effective in enhancing charge carrier separation and extending the light absorption range into the visible region [4,5]. Several studies have demonstrated that CuO/ZnO heterojunctions exhibit improved photocatalytic performance for hydrogen evolution and pollutant degradation due to their complementary electronic structures [6,7].In recent years, the incorporation of carbon-based materials, particularly ACR, has attracted considerable attention for further improving the performance of metal oxide photocatalysts. ACR, with its excellent electrical conductivity, large specific surface area, and high electron mobility, acts as an effective electron acceptor and transporter, suppressing recombination and enhancing photocatalytic activity [8,9]. Xu et al. (2018) reported that ACR/ZnO composites exhibited superior photocatalytic degradation of rhodamine B compared to pure ZnO, attributed to improved charge separation [10]. Similarly, Shaikh et al. (2021) demonstrated that the addition of ACR derivatives to CuO/ZnO photocatalysts significantly increased hydrogen evolution rates under visible light [11].

However, the role of ACR loading in such heterostructures is a critical factor. Low ACR content may not provide sufficient electron transfer pathways, while excessive ACR can lead to agglomeration and light-shielding effects, ultimately reducing the active surface area and photocatalytic efficiency [12]. Despite the growing interest, systematic studies focusing on the optimization of ACR content in CuO/ZnO composites for simultaneous solar hydrogen production and organic pollutant degradation are still limited.

In this context, the present study investigates the effect of varying ACR loadings on the structural, optical, and photocatalytic properties of CuO/ZnO nanocomposites. The composites were synthesized via a facile hydrothermal method and evaluated for their efficiency in hydrogen production from water splitting and the degradation of methylene blue under simulated solar irradiation. This work not only elucidates the influence of ACR content on dual photocatalytic

functions but also provides valuable insights into the design of multifunctional nanocomposites for sustainable energy and environmental applications.

MATERIALS AND METHODS

Materials

Copper(II) nitrate trihydrate [$Cu(NO_3)_2 \cdot 3H_2O$, 99%], zinc nitrate hexahydrate [$Zn(NO_3)_2 \cdot 6H_2O$, 99%], sodium hydroxide (NaOH) , potassium hydroxide , coconut shell, urea, sulfuric acid (H_2SO_4), methylene blue (MB) dye, and ethanol of analytical grade were purchased from Sigma-Aldrich and used without further purification. Deionized (DI) water was used in all synthesis and experimental procedures.

Synthesis of Activated Carbon Rings (ACR)

Activated carbon rings (ACR) were prepared using coconut shell as the carbon precursor and potassium hydroxide (KOH) as the chemical activating agent. Fresh coconut shells were initially washed several times with tap water followed by deionized water to remove adhering dust and soluble impurities and were then dried in a hot-air oven at 105°C for 24 hours. The dried shells were cut into small pieces, mechanically crushed, and sieved to obtain particles of 1-2 mm size. Approximately 100 g of the prepared coconut-shell particles was carbonized in a tubular furnace under a continuous nitrogen flow of 150 mL min-1. The temperature was increased from room temperature to 600°C at a heating rate of 5°C min-1 and maintained at 600 °C for 2 hours. After natural cooling to room temperature under nitrogen, the resulting char was collected, pulverized, and sieved to obtain particles below 250 μm. For chemical activation, 50 g of the carbonized char was impregnated with 100 g of KOH using a char-to-KOH mass ratio of 1:2. The mixture was dispersed in 250 mL of deionized water and continuously stirred at 80 °C for 4 h to obtain uniform impregnation. The resulting slurry was dried at 105 °C for 24 h and subsequently transferred to a tubular furnace for activation under nitrogen flow (150 mL min-1). The temperature was increased at 5 °C min-1 to 750 °C and maintained for 1 hour. After activation, the material was allowed to cool to room temperature under nitrogen. The activated carbon was washed initially with 0.1 M hydrochloric acid to remove residual potassium-containing inorganic species and subsequently washed several times with hot deionized water until the filtrate reached a pH of 6.5–7.0. The washed activated carbon was dried at 105 °C for 12 h. To fabricate the ring-shaped geometry, the activated carbon powder was mixed with 8 wt% starch binder and approximately 15 mL of deionized water per 100 g of activated carbon and kneaded for 30 min to obtain a homogeneous paste. The mixture was pressed through a stainless-steel ring die to produce cylindrical rings with an outer diameter of 10 mm, inner diameter of 5 mm, and height of 10 mm. The green rings were dried at 80 °C for 12 h and subsequently subjected to a stabilization treatment at 300 °C for 1 h under nitrogen, followed by heating to 600 °C at 5 °C min^{-1} and holding for 1 h to remove the binder and improve structural integrity. The resulting porous carbon rings were cooled under nitrogen, weighed, and designated as activated carbon rings (ACR).

Preparation of CuO/ZnO Heterostructure

CuO/ZnO nanocomposites were synthesized via a hydrothermal method. In a typical procedure, 0.1 M Cu $(NO_3)_2 \cdot 3H_2O$ and 0.1 M Zn $(NO_3)_2 \cdot 6H_2O$ were dissolved in 100 mL of DI water, followed by the addition of 0.2 M urea. The solution was stirred for 30 minutes and transferred to a Teflon-lined autoclave. The reaction was carried out at 120 °C for 10 hours. The precipitate was collected, washed with DI water and ethanol, and calcinated at 400°C for 3 hours to obtain CuO/ZnO heterostructures.

Synthesis of ACR/CuO/ZnO Nanocomposites

The ACR/CuO/ZnO composites with ACR loadings of 1 wt% were synthesized via a one-pot hydrothermal method [14]. The required amount of ACR was ultrasonically dispersed in 50 mL DI water for 30 minutes. Cu $(NO_3)_2 \cdot 3H_2O$ and Zn $(NO_3)_2 \cdot 6H_2O$ were then added to the dispersion, followed by the addition of urea. The solution was transferred to an autoclave and heated at 120 °C for 10 hours. After cooling, the solid product was collected, washed with DI water and ethanol, and dried at 80 °C. Finally, the composites were calcinated at 400 °C in an aACRn atmosphere for 2 hours .

Table 1 Experimental parameters and Composition of Synthesized Photocatalyst Samples

Sample	S1	S2	S3	S4
ACR per total solid content (wt %)	1	1	1	100
CuO/ ZnO(1:1 wt%) per total solid content (wt %)	99	99	99	0
Material Composition	Binary composite with ZnO ACR/ZnO	Binary composite with CuO ACR/CuO	Ternary composite with ZnO and CuO ACR/CuO /ZnO	Pure ACR (control sample)

Characterization of materials

The crystal structure of the samples was characterized using a Rigaku Smart Lab 9 kW X-ray diffractometer with (λ = 0.15418 Å) Cu Kα radiation. Measurements were taken across angles ranging from 10 to 80 degrees. A unique five-axis

θ-θ goniometer provided precise structural analysis. Field emission scanning electron microscopy (FE-SEM) revealed the diverse morphologies of the synthesized materials. An FE-SEM TESCAN MAIA3 model, equipped with EDX capabilities, visualized the varied shapes and compositions at high resolution. Fourier transform infrared spectroscopy analyzed the characteristic functional groups within the materials. A BRUKER ALPHA-II FT-IR spectroscopically probed wavelengths from 500 to 4000 cm-1 inside a dehumidified chamber, removing interfering hydroxyl signals. A Hitachi F7000 spectrofluorometer (Hitachi High-Tech Corporation) was used to examine steady-state photoluminescence, utilizing an excitation wavelength of 250 nm. A Motras Double Beam UV-Vis Spectrophotometer with a wavelength accuracy of ± 0.1 nm and a spectral range of 200–1000 nm was used to conduct the UV-Vis investigation.

Photocatalytic Hydrogen Production Activity

Photocatalytic hydrogen evolution tests were conducted under UV irradiation using a gas circulation system. A 300 W Xenon lamp (Cermax PE300BF, 20 A) was employed as the light source. The system was vented with AACRn (Ar) gas for 30 min to promote an anoxic media to prevent oxygen from recombining with H_2 or consuming photogenerated electrons. Typically, 0.5 g of the photocatalyst was suspended in a solution containing 50 mL of water and 15 mL of methanol, with 0.5 wt % Pt added as a co-catalyst. To achieve a uniform dispersion, the mixture underwent ultrasonic treatment for 45 minutes before being transferred into a quartz reactor integrated with an online trace gas analysis system. Photocatalytic H_2 generation was initiated by irradiating the reactor with the Xenon lamp, equipped with a long-pass cut-off filter ($\lambda > 420$ nm). The evolved hydrogen was quantified using a gas chromatograph (GC-9200, China) fitted with an MS-5A zeolite column and a thermal conductivity detector (TCD), employing aACRn (Ar) as the carrier gas in every 30 min. The average values and error bars are calculated based on three independent experiments to ensure accuracy. The hydrogen production rate was expressed in $\mu mol\ g^{-1}\ h^{-1}$.

Photocatalytic Degradation of Organic Dye

Photocatalytic degradation of methylene blue (MB) was evaluated under simulated solar irradiation using a 300 W Xenon lamp. In each test, 50 mg of catalyst was dispersed in 100 mL of 10 mg/L MB solution. Prior to irradiation, the suspension was magnetically stirred in the dark for 30 minutes to achieve adsorption–desorption equilibrium. Aliquots (5 mL) were withdrawn at regular intervals during irradiation, centrifuged, and analyzed using a UV–visible spectrophotometer (Shimadzu UV-2600) at $\lambda\_max = 664$ nm.

RESULTS AND DISCUSSION

XRD Analysis

The crystalline structure of the synthesized CuO/ZnO and ACR-CuO/ZnO photocatalysts was confirmed by X-ray diffraction (XRD) analysis (Figure 3). Distinct diffraction peaks at $2\theta = 31.7°$, 34.4°, 36.2°, 47.5°, and 56.6° were indexed to the (100), (002), (101), (102), and (110) planes of hexagonal wurtzite ZnO (JCPDS No. 36-1451). Additionally, peaks observed at 32.5°, 35.5°, 38.7°, 48.7°, 53.4°, and 58.3° correspond to the (110), (-111), (111), (-202), (020), and (202) planes of monoclinic CuO (JCPDS No. 48-1548), indicating successful formation of the composite. Figure 5 displays peaks that could be related to ACR at 26.1° (002) and 42.9° (100). Additionally, the characteristic GO peak at 10.7° (001) vanishes from sight from the composite pattern. These findings demonstrated that ACR was effectively transformed to ACR.

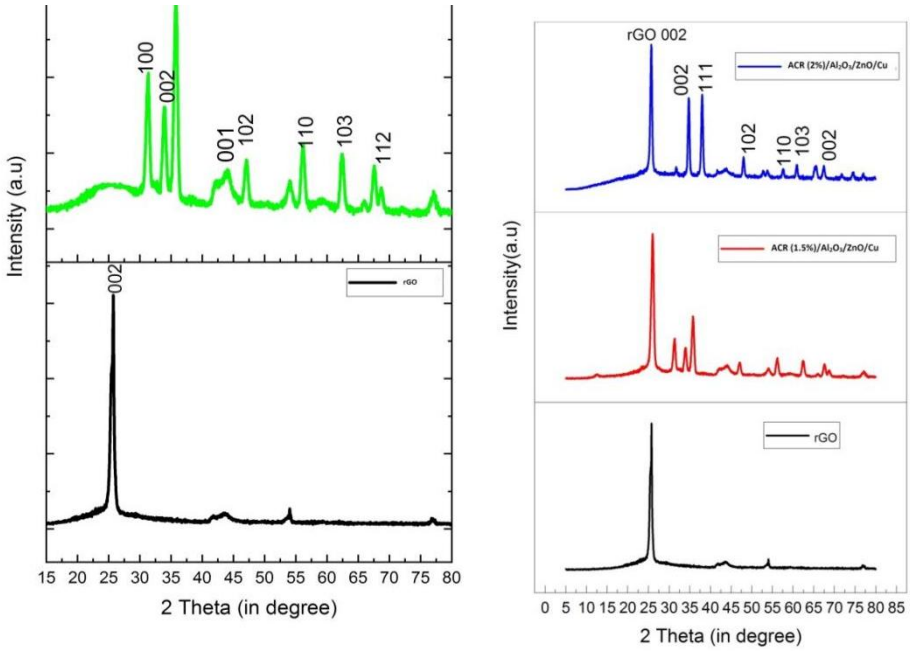

Figure 1(a,b). XRD patterns of different samples of ACR; ACR (1 %)/ZnO; ACR (1 %)CuO; ACR (1 %)/CuO/ZnO

Morphological and Elemental Analysis

The morphological and elemental characteristics of the synthesized photocatalysts were examined using SEM and EDX analyses. Scanning electron microscopy (SEM) was conducted to examine the surface morphology and structural

distribution of the synthesized photocatalysts. Figure 3 displays the SEM visualization of reduced ACR, highlighting it's distinctly wrinkled and crumpled surface. The ACR sheets appear to be thin, transparent, and layered as a result of the reduction process that converts GO into ACR

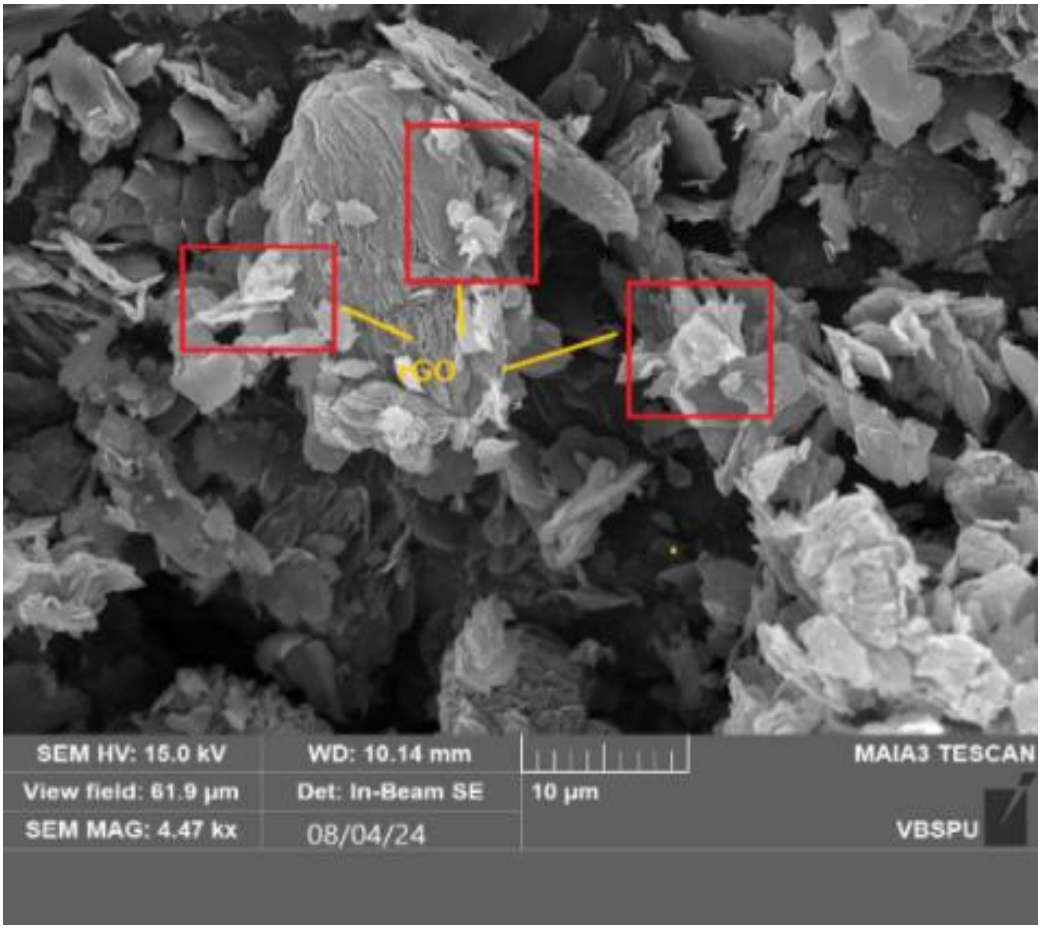

Figure 2. SEM image of ACR

The EDX spectra of Samples 1 to 3 provided clear elemental signatures corresponding to the constituent materials. The SEM and EDX images of Samples 1 to 3 are shown in Figure 3(a–o) Sample 1 (ACR–ZnO), shown in Figure 5(a–d), exhibits a uniform dispersion of ZnO nanoparticles over the wrinkled and layered structure of ACR sheets. The close interfacial contact between ZnO and the ACR matrix is indicative of effective surface anchoring, which is essential for enhancing electron mobility and reducing recombination in photocatalytic processes [15]. Sample 1 (ACR/ZnO) showed prominent peaks corresponding to zinc (Zn) and oxygen (O) along with a significant signal for carbon (C), which originates from the ACR sheets. The Kα lines of each element are represented by separate peaks in the EDX spectrum. ZnO is present because the Zn Kα peak, which is significant, is located at 8.65 keV and 1.11 keV and O Kα = 0.52 keV, along with a prominent C Kα peak at 0.28 keV as shown in figure 5(e). Sample 2 (ACR/CuO), displayed in Figure 5(f–i), presents a mixed morphology characterized by the presence of CuO nanorods and nanoplate-like structures embedded within the ACR framework. The CuO structures appear moderately aggregated yet well-integrated with the ACR sheets, suggesting strong interfacial interaction. Such interaction not only stabilizes the metal oxide particles but also enhances charge transfer capabilities across the composite. Sample 2 (ACR/CuO) displayed distinct EDX peaks for copper (Cu) and oxygen (O), along with carbon (C) from the ACR. The inclusion of CuO is verified by the peak, which appears around 0.93 keV (Lα), 8.04 keV (Kα), and 8.95 keV (Kβ), O Kα = 0.52 keV, and C Kα = 0.28 keV [16] as shown in figure 5(j). Sample 3 (ACR/ZnO/CuO), illustrated in Figure 5c, reveals a well-distributed, hybrid microstructure with both ZnO and CuO nanoparticles anchored homogeneously onto the ACR scaffold. The ternary configuration leads to the formation of a compact and interconnected network, where the presence of dual semiconductors promotes the establishment of multiple heterojunctions. This structural arrangement is expected to facilitate efficient charge carrier separation and migration, thereby enhancing the overall photocatalytic performance under solar irradiation. In Sample 3 (ACR/CuO /ZnO), all expected elemental peaks were identified, including Zn Kα (8.63 keV), Cu Kα (8.04 keV), O Kα (0.52 keV), and C Kα (0.28 keV) [17]. The simultaneous detection of both metal elements, without evidence of unwanted impurities, validates the successful synthesis of the ternary composite and supports the formation of a ZnO-CuO heterojunction on the ACR substrate.

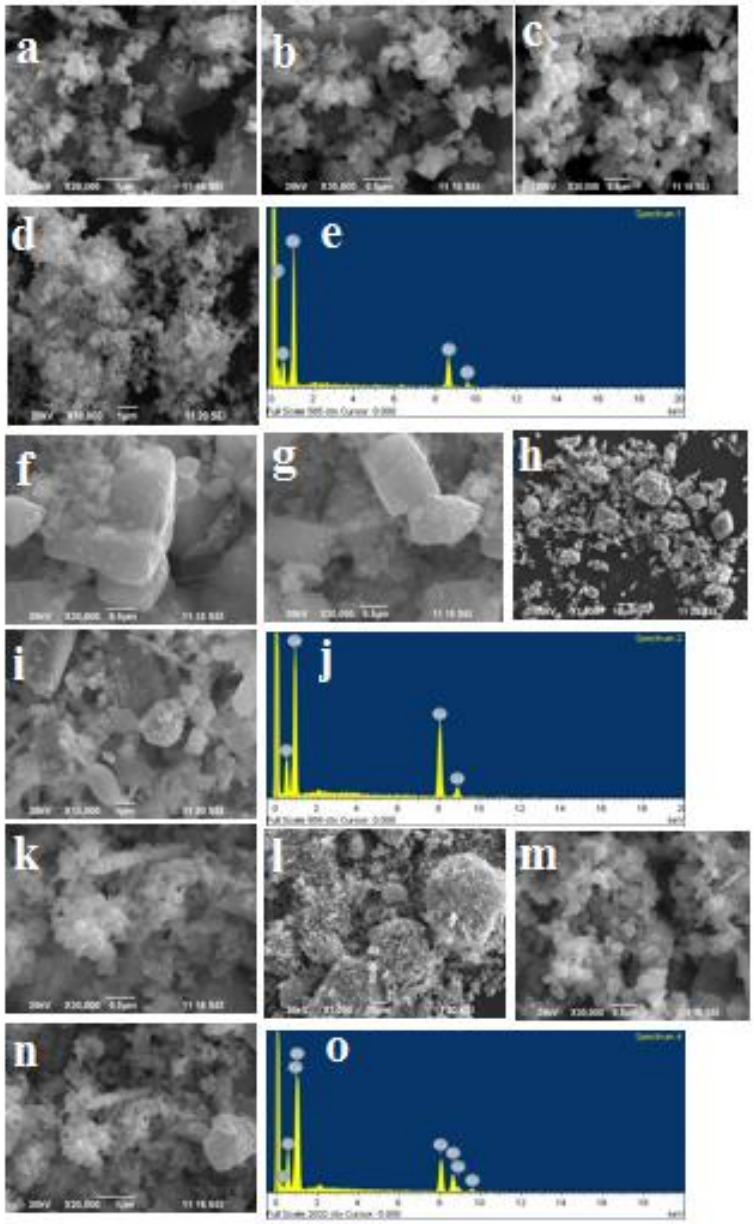

Figure 3 SEM and EDX images of different synthesized samples of (a-e) ACR (1 %)/ZnO (f-j) ACR (1 %)/CuO, (k-o) ACR(1 wt%)/CuO/ZnO

UV–Vis Spectroscopy

The optical properties of the synthesized samples were analyzed using UV-Vis absorption spectroscopy to investigate the electronic transitions and band structure modifications induced by the incorporation of ZnO, CuO, and ACR. The absorption spectra of Sample 1 (ACR(1%)/ZnO), Sample 2 (ACR(1%)/CuO), Sample 3 (ACR(1%)/ZnO/CuO), and Sample 4 (ACR) are presented in Figure 4 (a). Sample 4, consisting of pure ACR, exhibited a characteristic absorption peak at approximately 285 nm, corresponding to the $\pi \rightarrow \pi*$ transition of sp^2 hybridized carbon domains. This redshift from pristine ACR (typically observed at ~230 nm) confirms the successful reduction process and partial restoration of the conjugated carbon network. For Sample 1 ACR (1%)/ZnO, a distinct absorption edge was observed around 315 nm, which corresponds to the intrinsic band gap absorption of ZnO. The presence of ACR broadened the absorption spectrum, indicating enhanced light absorption due to the interaction between ZnO and ACR. Similarly, Sample 2 (ACR(1%)/CuO) exhibited an absorption feature near 274 and 320 nm, attributed to the band gap transition of CuO. The extended absorption range suggests improved light-harvesting properties due to the coupling between CuO and ACR. Notably, Sample 3 (ACR(1%)/ZnO/CuO) demonstrated a synergistic effect, with a broad absorption profile covering the UV-visible region. The absorption edge was observed in the range of 347 nm [18], which can be attributed to the combined contributions of ZnO and CuO, as well as the enhanced charge transfer interactions facilitated by ACR. The broadened absorption and redshifted edge in Sample 3 indicate improved light utilization, which is beneficial for photocatalytic applications.

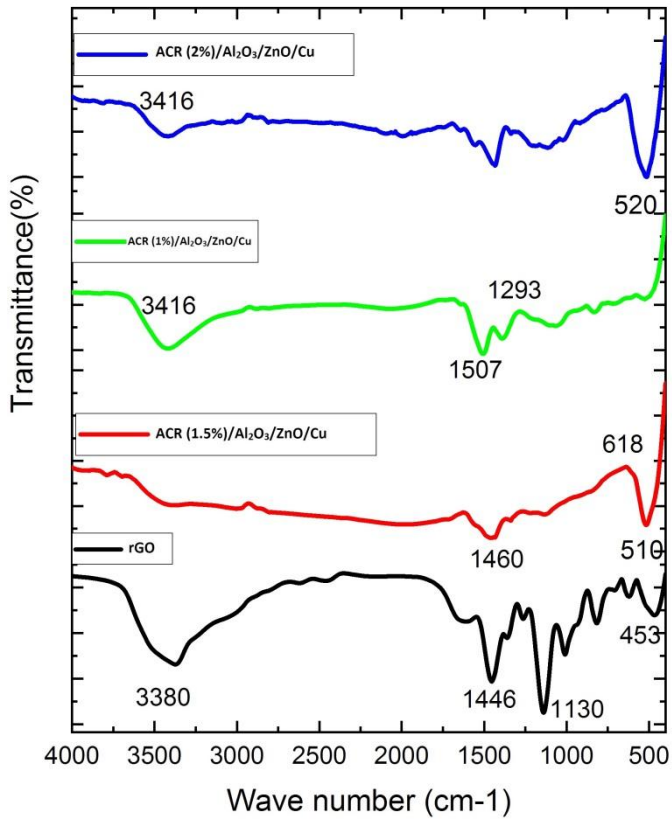

(a)

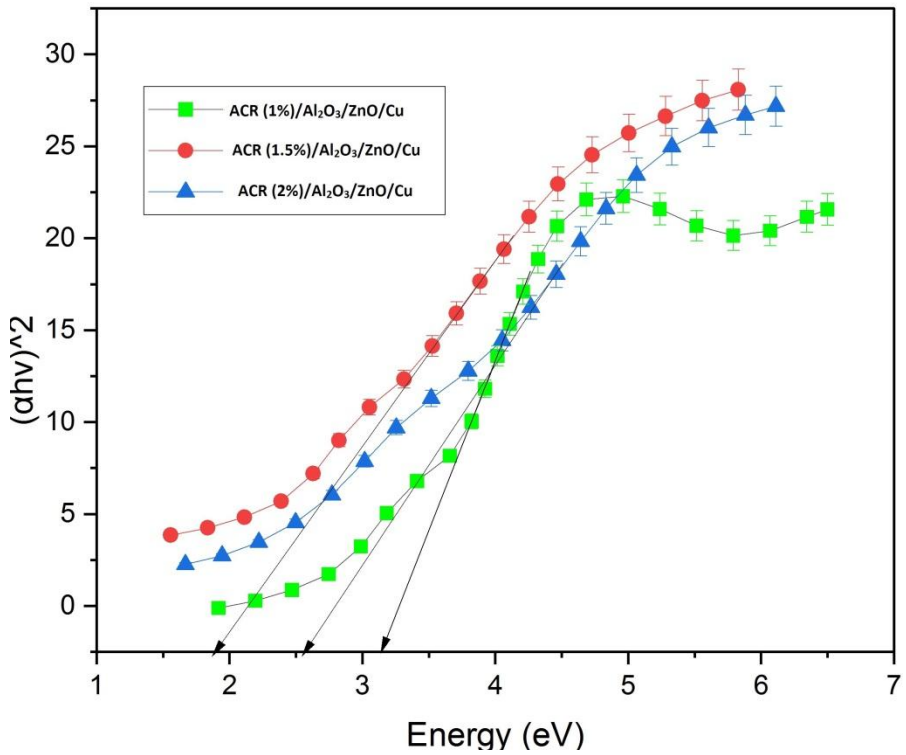

(b)

Figure 4. (a) UV- Vis spectra of different synthesized samples of ACR (1 %); ACR (1 %)/ZnO; ACR (1 %)/CuO; ACR(1 wt%)/CuO/ZnO (b) Tauc plots (Energy band-gap calculation) of different synthesized samples. The error bars show standard deviations of experimental results

Band-gap energies could be estimated using tauc plots, which examine the correlation between the absorption coefficient (α) and photon energy (hv). Figure 4 (b) shows band-gap energy (Eg) for different samples (S1, S2, and S3) and were found to be 3.20 eV, 1.90 eV and 2.34 eV. ZnO's band-gap energy was determined to be 3.2 eV, whereas the band-gap energy of copper oxide was assessed to be 2.5eV. The band gap energy of sample (S3) is reduced to approximately 2.34 eV, indicating enhanced photocatalytic activity due to improved light absorption capacity.

FT-IR Analysis

Fourier-transform infrared (FT-IR) spectroscopy was conducted to analyze the functional groups present in the synthesized nanocomposites and to confirm the successful integration of ZnO and CuO with ACR. FT-IR analysis confirms the successful synthesis of ACR-metal oxide nanocomposites and highlights the strong interfacial interactions between ACR, ZnO, and CuO. These interactions play a crucial role in improving the electronic and photocatalytic properties of the materials,The FT-IR spectra of Sample 1 (ACR(1%)/ZnO), Sample 2 (ACR(1%)/CuO), Sample 3 (ACR(1%)/ZnO/CuO), and Sample 4 (ACR) are presented in Figure 5. Sample 4, consisting of pure ACR, exhibited characteristic absorption bands at ~3440 cm-1, corresponding to the O–H stretching vibrations of residual hydroxyl groups, and at ~1478 cm-1, associated with the C=C stretching of sp^2 hybridized carbon domains. Peak at ~2930 cm-1, associated with the C-H stretching of carbon and hydrogendomains. The presence of weak peaks around ~1720 cm-1 and ~1125 cm-1 can be attributed to residual carboxyl (C=O) and epoxy (C–O) groups, respectively, indicating that the reduction of ACR was incomplete. For Sample 1 (ACR/ZnO), the FT-IR spectrum revealed additional vibrational bands around ~509 cm-1, which are characteristic of Zn–O stretching modes. The appearance of these peaks confirms the successful incorporation of ZnO nanoparticles onto the ACR matrix [19]. A reduction in the intensity of oxygen-containing functional groups (O–H, C=O, and C–O) suggests a strong interaction between ZnO and ACR, which may facilitate effective charge transfer. In Sample 2 (ACR/CuO), prominent absorption bands were observed around ~511 cm-1 corresponding to Cu–O stretching vibrations. The peaks associated with C=O and O–H functionalities exhibited reduced intensity compared to pure ACR, indicating effective anchoring of CuO onto the ACR surface. The presence of both CuO-related peaks and characteristic ACR bands confirms the formation of the composite. Sample 3 (ACR/ZnO/CuO) exhibited a combination of vibrational modes corresponding to both ZnO and CuO. The presence of distinct Zn–O and Cu–O stretching bands in the ~505 cm-1 region confirmed the coexistence of both metal oxides within the composite. Additionally, a further decrease in the intensities of the oxygen-containing functional groups (O–H, C=O, and C–O) suggests enhanced interaction between ACR and metal oxides, potentially improving electron mobility and catalytic performance.

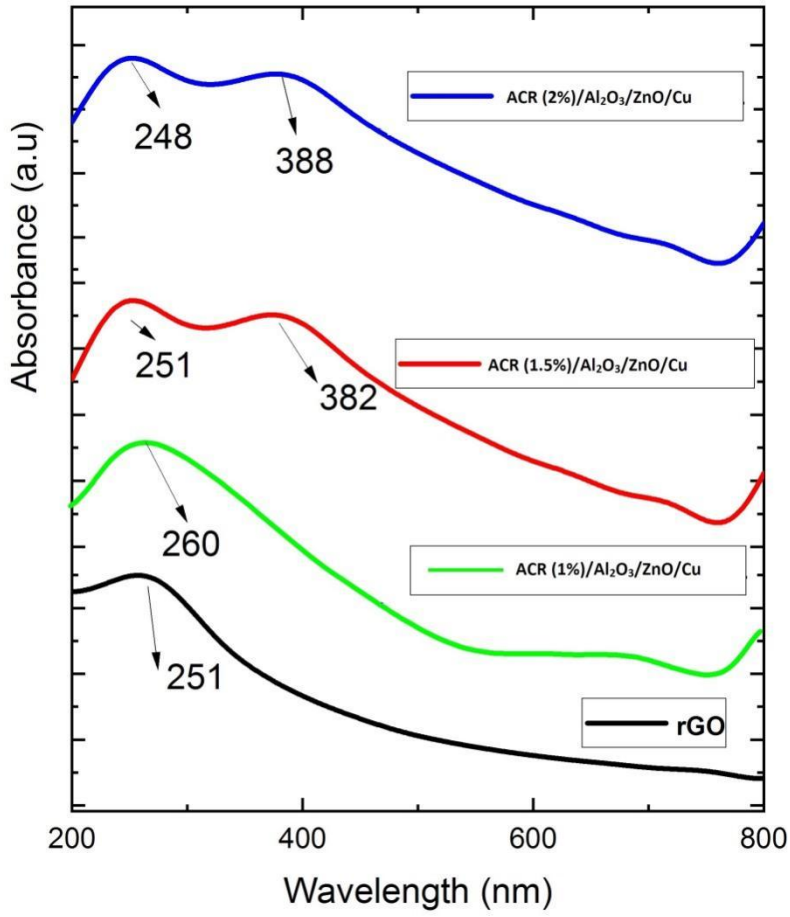

Figure 5. FT-IR pattern of different synthesized samples of ACR (1 %); ACR (1 %)/ZnO; ACR (1 %)/CuO; ACR(1 wt%)/CuO/ZnO

Photoluminescence (PL) spectroscopy was employed to investigate the charge carrier recombination behavior of the synthesized photocatalysts. The PL intensity provides qualitative insight into the separation efficiency of photogenerated electron-hole pairs; a lower PL intensity typically indicates more effective charge separation, which is critical for enhancing photocatalytic activity. PL spectra of ACR (1 wt. %) /CuO, ACR (1 wt. %) /ZnO, and ACR (1 wt. %) /CuO/ZnO nanocomposites were displayed in Figure 6. with emission bands centered prominently at approximately 280 nm and 517 nm. The intensity of these peaks reflects the rate of radiative recombination of photogenerated electron-hole pairs, which

inversely correlates with photocatalytic performance. ACR (1 %)/ZnO sample, showed higher PL intensity than ACR (1 wt%)/CuO, and ACR (1 wt%)/CuO/ZnO. This indicates relatively higher recombination of charge carriers, though the presence of ACR does contribute to a reduction in intensity compared to pure ZnO. ACR (1 %)/CuO, exhibited intermediate PL intensity. Although CuO has a narrower band gap and inherently lower recombination rates compared to ZnO [20], the incorporation of ACR further aids in reducing PL intensity by facilitating charge delocalization across the ACR matrix. Sample ACR(1 %)/CuOZnO, displayed the lowest PL intensity among all samples. This significant quenching effect is attributed to the efficient charge separation and transfer facilitated by the formation of a heterojunction between ZnO and CuO, with ACR serving as an excellent electron conductor. The suppressed PL signal indicates a reduced recombination rate of photo induced charge carriers, which is crucial for enhancing both photocatalytic hydrogen production and dye degradation efficiency.

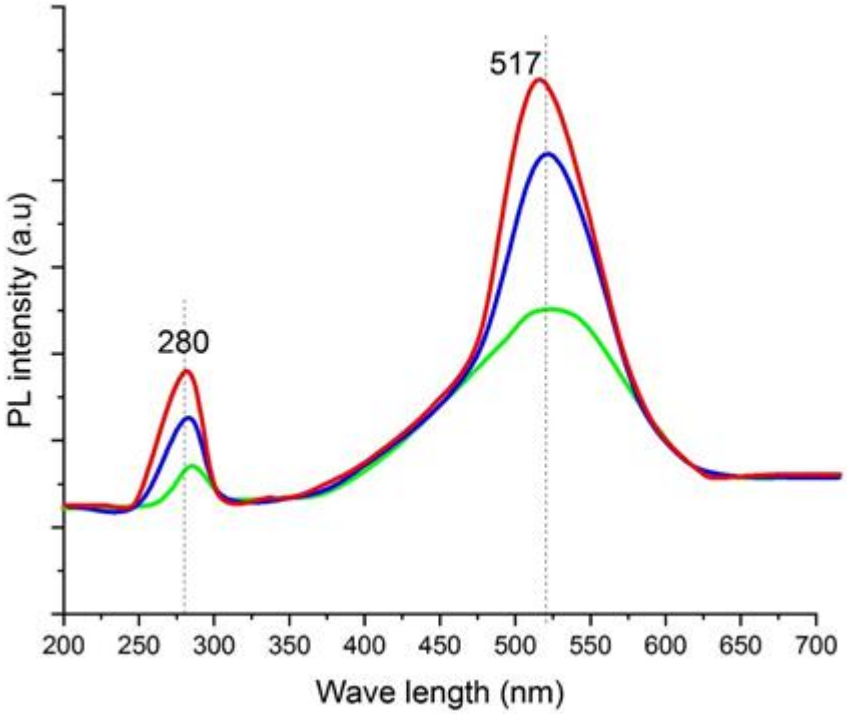

Figure 6.Photoluminescence spectrum of different samples of ACR (1 %)/ZnO; ACR (1 %)/CuO; ACR(1 wt%)/CuO/ZnO

Photocatalytic Performance Activity

The photocatalytic degradation efficiency of prepared nanocomposite samples were investigated under 300W visible light illumination using the model pollutant. For this experiment, 5 g of each synthesized catalyst was dispersed in 100 mL of aqueous MB solution, followed by continuous stirring under visible light for thirty minutes. UV-visible absorption spectra were collected every 10 minutes to evaluate and track the degradation efficiency of the materials.

Photocatalytic degradation percentage

%D = ((Co-Ct)/Co) x 100

Here, Co stands for the dye solution's starting concentration and Ct for the dye concentration at 10-minute intervals throughout the photocatalytic process.

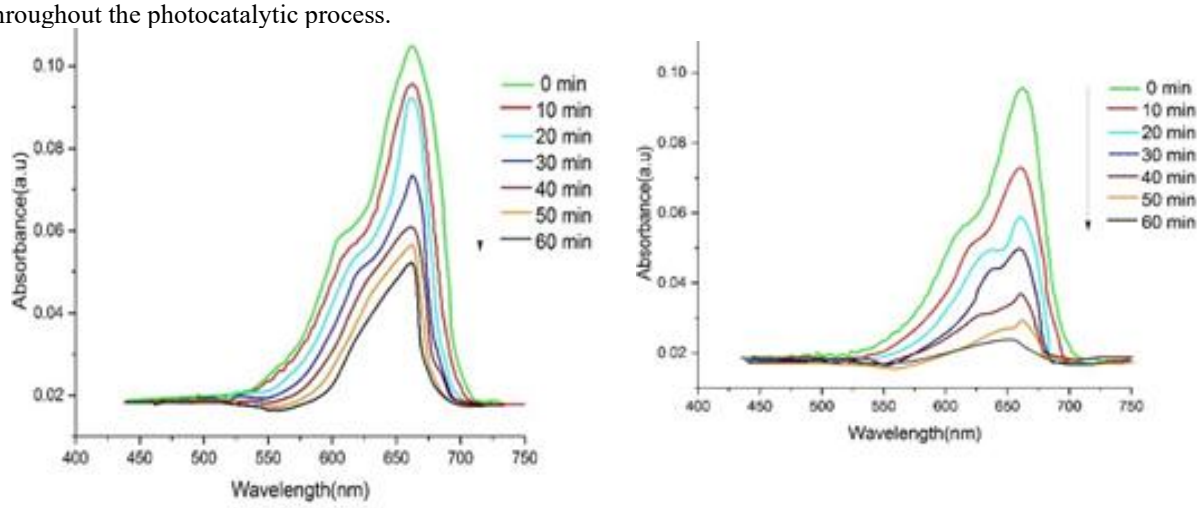

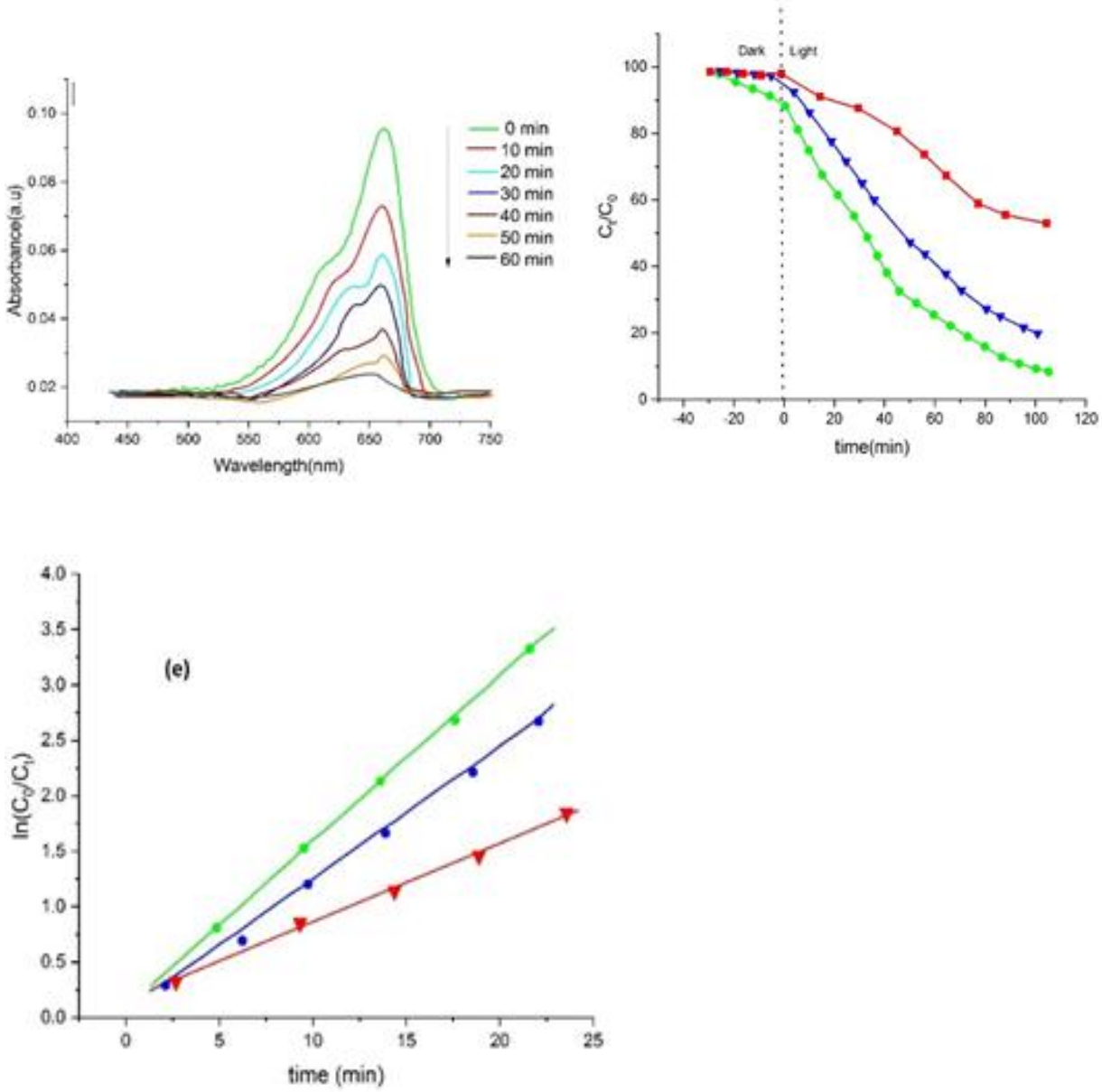

Figure7 Time-dependent photocatalytic degradation using catalysts: (a) ACR (1 %)/ZnO (b) ACR (1 %)/CuO (c) ACR(1 wt%)/CuO/ZnO; (d) Graphs of Ct/C0 versus time; (e) Graphs of ln(Ct/C0) versus time

Figure 7(a-c) displays the aqueous MB solution's absorption spectra at different time intervals. A prominent absorbance peak was observed at 670 nm in the MB aqueous solution [21]. The absorbance of the MB solution with catalysts progressively decreased under irradiation, indicating MB breakdown. The results explored that the ACR (1%)/ZnO nanocomposite aimed approximately 70% decomposition of the initial methylene blue (MB) concentration within 60 minutes. In comparison, the ACR (1 %)/CuO sample degraded around 80%, and the ACR(1 wt%)/CuO/ZnO sample exhibited the highest efficiency, degrading about 95% of the initial MB concentration in the same timeframe. The Langmuir-Hinshelwood model and pseudo-first-order kinetics are commonly employed to evaluate the effect of the initial concentration of methylene blue (MB) in aqueous solutions on photocatalytic degradation kinetics at low MB concentrations. The pseudo-first-order reaction kinetics can be mathematically represented as:

$Ct=Coe-kt$

The linearized form of this equation is expressed as:

$\ln f_0(CoCt)= kt$

Where k denotes the pseudo-first-order reaction rate constant. The variation of $\ln f_0(CoCt)$ with irradiation time for different experimental conditions is depicted in Figure 7 (d & e), demonstrating an excellent linear fit across all trials. Based on the linear regression analysis, the rate constant (k) values were determined to be 0.015 min-1, 0.0258 min-1, and 0.0321 min-1 for ACR (1 %)/ZnO, ACR (1 %)/CuO, and ACR(1 wt%)/CuO/ZnO nanocomposites, respectively. The enhanced photocatalytic activity of the ACR (1 wt.%)/CuO/ZnO nanocomposite, suggests that the incorporation of ACR in CuO/ZnO heterojunction suppresses charge carrier recombination while improving visible light absorption.

Photocatalytic Hydrogen Evolution

Photocatalytic hydrogen (H_2) evolution was conducted under ultraviolet (UV) irradiation using a gas circulation system. A 300 W Xenon lamp (Cermax PE300BF, operating at 20 A) served as the light source. The experiment was performed in a closed quartz reactor to minimize external influences and ensure precise measurement of hydrogen evolution. A 0.5 g sample of the photocatalyst was dispersed in a mixed aqueous solution of 50 mL deionized water. In each experiment, 0.5 g of the photocatalyst was dispersed in 50 mL of aqueous solution containing 1:1, 1:3, and 1:5 vol% methanol as a sacrificial agent. Additionally, different co-catalysts such as 0.5 wt. % of platinum (Pt), gold (Au), Palladium (Pd), and copper (Cu) were introduced to enhance charge separation and catalytic efficiency in separate experiments. To achieve a uniform dispersion, the solution was subjected to ultrasonic treatment for 45 minutes before transferring it into the reactor. To initiate the photocatalytic reaction, the suspension was exposed to xenon lamp irradiation with a long-pass cut-off filter ($\lambda > 420$ nm). The quartz reactor was connected to an on-line trace gas analysis system to monitor hydrogen evolution. AACRn gas was used as a carrier, ensuring an inert atmosphere to prevent undesired side reactions. The hydrogen evolved during the reaction was quantified using a gas chromatograph (China, GC-9200) equipped with an MS-5A zeolite column and a thermal conductivity detector (TCD). Each measurement was conducted three times to ensure reproducibility and accuracy. The results demonstrated a stable and significant hydrogen evolution rate under UV irradiation. The optimized CuO/ZnO photocatalyst modified with reduced ACR exhibited a maximum H_2 evolution rate. The steady-state hydrogen evolution rate, at which hydrogen is consistently produced per hour under optimized conditions is found to be 29,500 µmol/g-1h-1. The three independent measurements showed a standard deviation of ±3.56% confirming the reliability of the experimental setup and catalyst stability over prolonged operation. Figure 10 (b) illustrates the retention of hydrogen evolution activity (%) over 10 photocatalytic cycles, evaluating the stability and reusability of the optimized catalysts. ACR/ CuO/ZnO (Pt) exhibited the highest stability, retaining 91% of its initial activity after 10 cycles. indicating good photostability and resistance to photocorrosion. Gold (Au) and palladium (Pd) showed a slightly higher degradation rate, with final retention values of 89% and 87%, respectively. This suggests that while they facilitate electron transfer, their long-term stability is slightly lower than Pt. Copper (Cu) demonstrated the highest degradation rate, retaining only 82% of its initial activity after 10 cycles. This could be due to its higher susceptibility to oxidation or surface passivation, reducing its catalytic efficiency.

Three separate measurements of hydrogen generation were performed in order to quantify random errors, which are caused by erratic changes in the experimental setup. The random error was computed using the standard deviation of these repeated measurements. Systematic errors are caused by persistent biases in the measurement system, which are frequently driven by environmental factors, calibration offsets, or device restrictions. In this study, to ensure accuracy the instrument was regularly calibrated with certified gas standards. Despite these precautions, a systematic error of 2% was estimated based on the instrument's calibration specifications. Table 2 shows the overall uncertainty, which was estimated using the root sum square approach, which combined systematic and random errors [22].

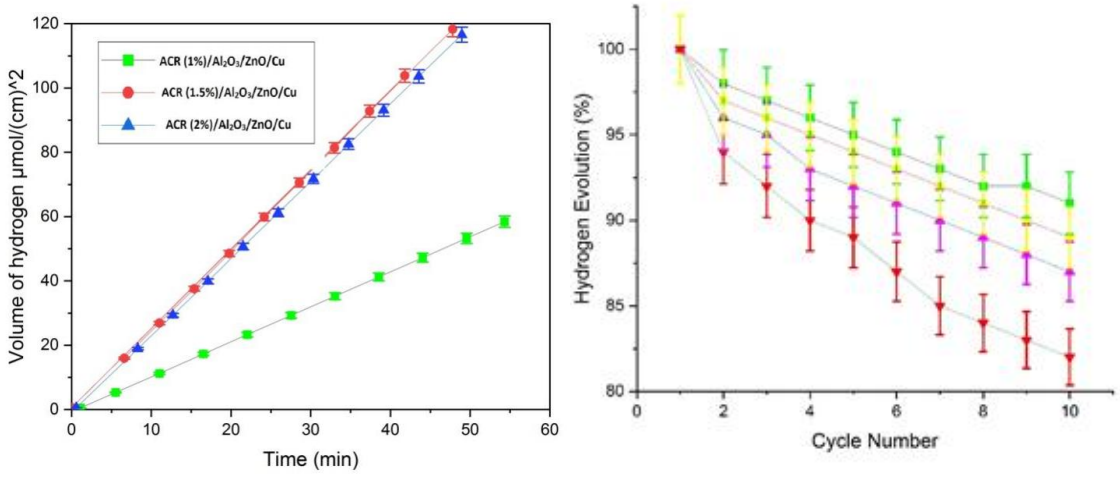

(a) (b)

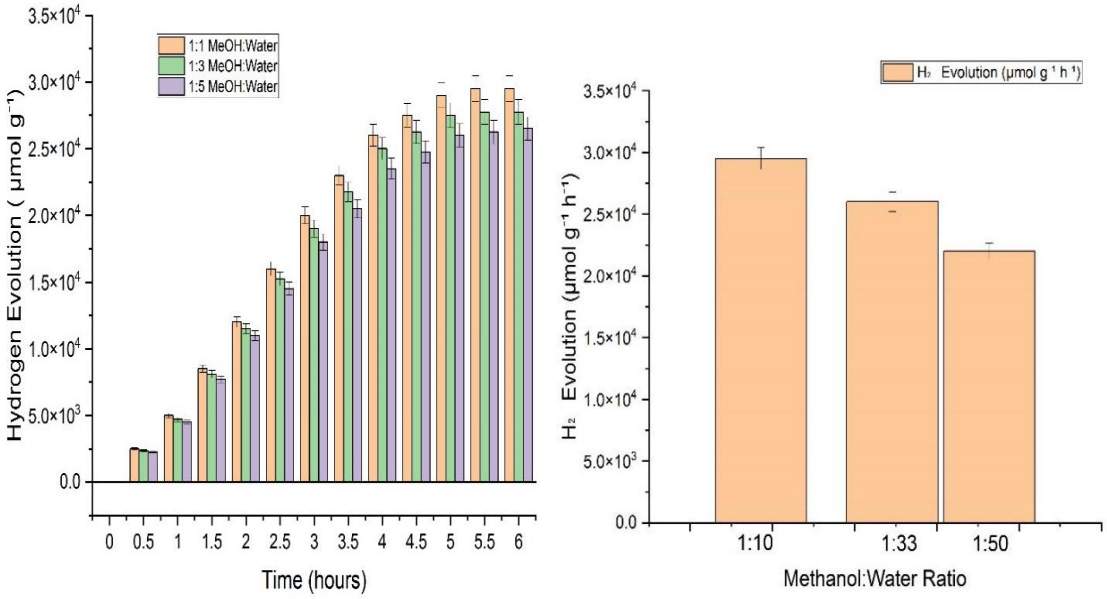

(c)

(d)

Figure 8 (a) Volume of hydrogen evolved versus time graph of different samples. The error bars show standard deviations of experimental results. (b) Stability Test over 10 Cycles for Different Catalysts (c) Time-dependent H2 evolution for different sacrificial agent ratios (1 wt% Pt) (d) bar graph representation comparing hydrogen evolution rates

Table 2 – Photocatalyst Composition, Co-Catalyst, Conditions, Band Gap, and H_2 Evolution

Catalyst	Band Gap (eV)	Co-Catalyst (wt%)	Sacrificial Agent	H_2 Evolution (µmol g^{-1} h^{-1})	Standard Deviation (Random error %)	Total Uncertainty (%)
ACR (1 %)/CuO	1.90	1% Pt	1:1 MeOH:H_2O	21,400	3.20%	3.80%
ACR (1 %) / ZnO	3.20	1% Pt	1:1 MeOH:H_2O	18,500	2.98%	3.58%
ACR (1 wt%) /CuO/ZnO	2.34	1% Pt	1:1 MeOH:H_2O	29,500	3.56%	4.12%
ACR (1 wt%) /CuO/ZnO	–	1% Au	1:1 MeOH:H_2O	25,000	3.20%	3.80%
ACR (1 wt%) /CuO/ZnO	–	1% Pd	1:1 MeOH:H_2O	22,000	2.98%	3.58%
ACR (1 wt%) /CuO/ZnO	–	1% Cu	1:1 MeOH:H_2O	15,000	3.20%	3.80%

CONCLUSIONS

This study successfully demonstrated the synthesis and evaluation of ACR modified CuO/ZnO photocatalysts for simultaneous solar hydrogen production and organic dye degradation. A comprehensive set of characterization techniques including XRD, FT-IR, UV-Vis, PL spectroscopy, SEM, and EDX confirmed the successful formation of binary and ternary nanocomposites with well-integrated and homogeneously dispersed CuO and ZnO nanoparticles on the ACR sheets. The inclusion of ACR effectively enhanced visible light absorption, facilitated charge carrier separation, and suppressed electron–hole recombination, as evidenced by reduced photoluminescence intensity. Among the synthesized materials, the ternary ACR/CuO/ZnO photocatalyst with 1 wt% ACR loading exhibited the highest performance, achieving a hydrogen evolution rate of 29,500 ± 1215.4 µmol g-1 h-1 and a methylene blue degradation efficiency of 95% within 60 minutes under simulated solar irradiation. Platinum (Pt) demonstrated the highest catalytic efficiency, while gold (Au) and palladium (Pd) also enhanced activity but to a lesser extent. Copper (Cu) resulted in the lowest performance (15,000 µmol g-1 h-1), likely due to its weaker electron transfer capability. The superior performance of Pt-modified ACR (1%)/CuO/ZnO with 1:1 sacrificial agent ratio makes it a promising candidate for photocatalytic water splitting applications. The reduced band gap and synergistic effect of the heterojunction structure significantly contributed to its superior photocatalytic activity.Stability and recyclability tests over 10 successive photocatalytic cycles revealed that the optimized ACR/CuO/ZnO nanocomposite retained 91% of its initial hydrogen production activity, indicating excellent photostability and resistance to photocorrosion. Furthermore, experimental error analysis confirmed the reproducibility

and reliability of the photocatalytic results, with minimal data fluctuations observed across repeated trials. This work highlights the critical role of optimized ACR loading in enhancing the photocatalytic efficiency of CuO/ZnO systems. The developed nanocomposite offers a promising, sustainable approach for integrated solar fuel generation and wastewater remediation.

REFERENCES

1. S. Dubey and S. K. Singh, "Role of reduced graphene oxide in promoting photocatalytic H_2 evolution over CuO/ZnO catalyst," Int. J. Energy Clean Environ., vol. 27, no. 5, pp. 59–73, 2026, doi: 10.1615/InterJEnerCleanEnv.2025057236.
2. S. Dubey and S. K. Singh, "Development of Al/CuO/ZnO/rGO nanocomposites for enhanced photocatalytic degradation of organic pollutants in wastewater treatment," J. Solid Waste Technol. Manage., vol. 51, no. 2, pp. 210–221, 2025, doi: 10.5276/jswtm/iswmaw/512/2025.210.
3. A. K. Pawan, S. Dubey, and S. K. Singh, "Fabrication and characterization of alumina-doped ZnO/CuO-CNT nanocomposites for enhanced solar-driven photocatalytic activity," J. Appl. Bioanal., vol. 11, no. 6S, pp. 320–328, Dec. 2025, doi: 10.53555/jab.v11si6.1682.
4. A. Fujishima and K. Honda, "Electrochemical photolysis of water at a semiconductor electrode," Nature, vol. 238, no. 5358, pp. 37–38, Jul. 1972, doi: 10.1038/238037a0.
5. M. A. Rauf and S. S. Ashraf, "Fundamental principles and application of heterogeneous photocatalytic degradation of dyes in solution," Chem. Eng. J., vol. 151, nos. 1–3, pp. 10–18, Aug. 2009, doi: 10.1016/j.cej.2009.02.026.
6. A. Kołodziejczak-Radzimska and T. Jesionowski, "Zinc oxide—from synthesis to application: A review," Materials, vol. 7, no. 4, pp. 2833–2881, Apr. 2014, doi: 10.3390/ma7042833.
7. R. S. Sonawane et al., "Solar photocatalytic hydrogen production using CuO–ZnO coupled oxide semiconductors," Int. J. Hydrogen Energy, vol. 33, no. 12, pp. 3117–3123, 2008.
8. K. Prasad and M. Srivastava, "A review on CuO based photocatalysts: Synthesis, characterization, and applications," J. Mater. Sci.: Mater. Electron., vol. 31, pp. 9146–9160, 2020, doi: 10.1007/s10854-020-03498-7.
9. B. V. Ayodele et al., "Recent advances in copper oxide-based photocatalysts for water splitting and environmental remediation," J. Environ. Chem. Eng., vol. 5, no. 6, pp. 6011–6028, 2017.
10. Z. Ma et al., "Construction of CuO/ZnO heterostructures with enhanced photocatalytic performance for hydrogen production," Appl. Surf. Sci., vol. 319, pp. 92–98, 2014.
11. G. Williams, B. Seger, and P. V. Kamat, "TiO_2–graphene nanocomposites: UV-assisted photocatalytic reduction of graphene oxide," ACS Nano, vol. 2, no. 7, pp. 1487–1491, Jul. 2008, doi: 10.1021/nn800251f.
12. H. Zhang et al., "Graphene-based composites as photocatalysts: A review," Energy Environ. Sci., vol. 5, no. 11, pp. 9773–9781, 2012, doi: 10.1039/C2EE21555A.
13. J. Xu et al., "Enhanced photocatalytic degradation of rhodamine B over ZnO–ACR composites: Mechanism and role of ACR," Mater. Res. Express, vol. 5, no. 9, Art. no. 095023, 2018, doi: 10.1088/2053-1591/aad63e.
14. S. Shaikh et al., "Enhanced hydrogen production from visible-light-driven water splitting over graphene-based CuO–ZnO photocatalysts," Int. J. Hydrogen Energy, vol. 46, no. 38, pp. 19691–19701, 2021.
15. S. Ghosh et al., "The impact of graphene oxide loading on ZnO-based nanocomposites for photocatalytic activity: Balancing between surface area and light shielding effect," J. Phys. Chem. C, vol. 122, no. 32, pp. 18422–18431, 2018, doi: 10.1021/acs.jpcc.8b04840.
16. H. Moussa, E. Girot, K. Mozet, H. Alem, G. Medjahdi, and R. Schneider, "ZnO rods/reduced graphene oxide composites prepared via a solvothermal reaction for efficient sunlight-driven photocatalysis," Appl. Catal. B: Environ., vol. 185, pp. 11–21, May 2016, doi: 10.1016/j.apcatb.2015.12.007.
17. S. Dubey and S. K. Singh, "Assessment of electromechanical performance of graphene-reinforced aluminum nanocomposites for energy storage solutions," Int. J. Mater. Sci. Technol., vol. 10, no. 1, pp. 1950–1958, Jun. 2023.
18. N. Kumaresan, M. M. A. Sinthiya, K. Ramamurthi, R. R. Babu, and K. Sethuraman, "Visible light driven photocatalytic activity of ZnO/CuO nanocomposites coupled with ACR heterostructures synthesized by solid-state method for RhB dye degradation," Arab. J. Chem., vol. 13, no. 2, pp. 3910–3928, 2020, doi: 10.1016/j.arabjc.2019.03.002.
19. H. Qin, W. Li, Y. Xia, and T. He, "Photocatalytic activity of heterostructures based on ZnO and N-doped ZnO," ACS Appl. Mater. Interfaces, vol. 3, no. 8, pp. 3152–3156, 2011, doi: 10.1021/am200655h.
20. K. Tantubay, K. S. Devi, and M. Baskey, "Ternary reduced graphene oxide–CuO/ZnO nanocomposite as a recyclable catalyst with enhanced reducing capability," J. Environ. Chem. Eng., vol. 8, no. 5, Art. no. 103818, Oct. 2020, doi: 10.1016/j.jece.2020.103818.
21. R. A. Basit, Z. Abbasi, M. Hafeez, P. Ahmad, J. Khan, M. U. Khandaker, K. S. Al-Mugren, and A. Khalid, "Successive photocatalytic degradation of methylene blue by ZnO, CuO, and ZnO/CuO synthesized from Coriandrum sativum plant extract via green synthesis technique," Crystals, vol. 13, no. 2, Art. no. 281, Feb. 2023, doi: 10.3390/cryst13020281.
22. R. Saravanan, S. Karthikeyan, V. K. Gupta, G. Sekaran, V. Narayanan, and A. Stephen, "Enhanced photocatalytic activity of ZnO/CuO nanocomposite for the degradation of textile dye on visible light illumination," Mater. Sci. Eng. C, vol. 33, no. 1, pp. 91–98, Jan. 2013, doi: 10.1016/j.msec.2012.08.011.